

Energetic neutral atoms around HD 209458b: Estimations of magnetospheric properties

A. Ekenbäck and M. Holmström

Swedish Institute of Space Physics, PO Box 812, SE-98128 Kiruna, Sweden

`andreas@irf.se`

P. Wurz

Physikalisches Institut, University of Bern, Sidlerstr. 5, CH-3012 Bern, Switzerland

J-M. Grießmeier

*Netherlands Institute for Radio Astronomy, Oude Hoogeveensedijk 4, NL-7991 PD Dwingeloo,
The Netherlands*

H. Lammer

Space Research Institute, Austrian Academy of Sciences, Schmiedlstr. 6, A-8042 Graz, Austria

F. Selsis

Laboratoire d'Astrophysique de Bordeaux, Université Bordeaux 1, BP 89, F-33270, Floirac, France

and

T. Penz

INAF – Osservatorio Astronomico di Palermo, Piazza del Parlamento 1, I-90134 Palermo, Italy

ABSTRACT

HD 209458b is an exoplanet found to transit the disk of its parent star. Observations have revealed a large population of high-velocity atomic hydrogen around the "hot Jupiter" HD 209458b during transit. This work expands on an earlier work studying the production of energetic neutral atoms (ENAs) as a result of the interaction between the stellar wind and the exosphere. We present an improved flow model that, together with stellar wind values similar to the ones in our solar system, further supports that the observed hot hydrogen are ENAs. We also study how the production of ENAs depends on the exospheric parameters, and establish an upper limit for the obstacle standoff distance at approximately 4-10 planetary radii. Finally we compare the results obtained for the obstacle standoff distance with existing exomagnetospheric models, and show how the magnetic moment of HD 209458b can be estimated from ENA observations for different exospheric scenarios.

1. INTRODUCTION

HD 209458b is a Jupiter-type planet for which several transits in front of its parent star were discovered in 2000 (Charbonneau et al. 2000; Henry et al. 2000). Observations with the Hubble Space Telescope (HST) show absorption in the Lyman- α line (at 1215.67 Å) during transit, revealing the occurrence of high-velocity atomic hydrogen around HD 209458b (Vidal-Madjar et al. 2003). This has been interpreted as hydrogen atoms in the exosphere undergoing hydrodynamic escape, further accelerated by the stellar radiation pressure (Vidal-Madjar et al. 2003; Vidal-Madjar et al. 2004). Recently an alternative explanation was suggested by Holmström et al. (2008), hereafter H08, showing that energetic neutral atoms (ENAs) created by charge-exchange between the stellar wind and the exosphere can explain the observations. ENAs resulting from the interaction of the solar wind with a planetary environment have been observed at Earth (Collier et al. 2001), Mars (Futaana et al. 2006) and Venus (Galli et al. 2008), and charge-exchange with stellar wind protons around HD 209458b can explain the high-velocity hydrogen in analogy with these observations in our solar system. Here we study how an improved flow model for the stellar wind will affect the ENA production. In particular, the changes to the flow model are:

1. Stellar wind protons are now reflected at the obstacle boundary to model the deflected stellar wind flow around the obstacle. In the earlier model the protons arriving at the obstacle boundary were deleted.
2. The forces on hydrogen atoms in H08 were inaccurate at large distances from the planet since only the Coriolis force from the rotating coordinate system represented the gravity of the star. Star gravity and centrifugal force on the particles are now included.

We also investigate if it is possible to infer properties of the planetary obstacle to the stellar wind from the ENA observation, e.g. if the planet is magnetized or not.

2. THE SIMULATION MODEL

In what follows, the coordinate system used is centered at the planet and has its x -axis toward the star, the y -axis opposite the planet’s orbital velocity v_p , and the z -axis completes the right handed coordinate system. The default values of physical constants and parameters used in the simulation are listed in Table 1. Default values of numerical parameters can be found in Table 2.

The outer boundary of the simulation domain is the box $x_{\min} \leq x \leq x_{\max}$, $y_{\min} \leq y \leq y_{\max}$, and $z_{\min} \leq z \leq z_{\max}$. The inner boundary is a sphere of radius R_0 .

The conic obstacle to the stellar wind protons is defined by the surface (X, ρ) , such that $X = -\rho^2/(20R_p) + X_0$ where R_p is the planet’s radius, and X_0 is the obstacle stand off distance. Here ρ is the distance to the planet–star line, aberrated by an angle of $\arctan(v_p/v_{\text{sw}})$ to account

for the finite stellar wind speed v_{sw} relative to the planet’s orbital speed v_p . The location of the obstacle boundary along with the stellar wind direction and the orbital velocity direction are shown in Figure 1.

At the start of the simulation the domain is void of particles. Then hydrogen meta-particles are launched from the inner boundary at a rate of 300 meta-particles per second. Each meta-particles corresponds to N_m hydrogen atoms. The location on the inner boundary of each launched particle is randomly drawn with a probability proportional to the local hydrogen exobase density. The velocity of each launched particle is randomly drawn from a probability distribution proportional to

$$(\mathbf{n} \cdot \mathbf{v}) e^{-a|\mathbf{v}|^2},$$

where \mathbf{n} is the local unit surface normal, \mathbf{v} is the velocity of the particle, and $a = m/(2k_B T)$, m is the mass of a neutral, k_B is Boltzmann’s constant, and T is the temperature (at the exobase position). The distribution used is not Maxwellian, but the distribution of the flux through a surface (the exobase), given a Maxwellian distribution at the location (Garcia 2000). The number flux through the surface is $n/\sqrt{4\pi a}$, where n is the inner boundary hydrogen density, for a total production rate of $nR_0^2\sqrt{8\pi k_B T/m}$. After an hydrogen atom is launched from the inner boundary, we numerically integrate its trajectory with a time step of 25 seconds.

Before each time step we also fill the x -axis shadow cells (cells just outside the simulation domain) with proton meta-particles of the same weight as for hydrogen, N_m . After each time step the shadow cells are emptied of protons. The protons are drawn from a Maxwellian distribution with temperature T_{sw} and bulk velocity v_{rel} . The relative velocity at the planet, v_{rel} , is related to the stellar wind velocity and the planet’s orbital velocity by $v_{\text{rel}}^2 = v_{\text{sw}}^2 + v_p^2$. At the obstacle the stellar wind is reflected in the surface normal. The boundary conditions in the y - and z -directions are periodic.

The total number of meta-particles at the final time is approximately $9 \cdot 10^6$ of which $4 \cdot 10^6$ are hydrogen.

Between time steps, the following events can occur for an exospheric atom

- Collision with an UV photon. Following Hodges (1994) this occurs as an absorption of the photon – Δv opposite the star direction – followed by isotropic reradiation – Δv in a random direction – where we use a velocity change $\Delta v = 3.27$ m/s. The collision rate is zero if the particle is in the shadow behind the planet.
- Photoionization by a stellar photon occurs at a rate of τ_1 when an exospheric hydrogen atom is outside the optical shadow behind the planet, and then the meta-particle is removed from the simulation.
- Charge-exchange with a stellar wind proton. If the hydrogen atom is outside the obstacle it can charge exchange with a stellar wind proton, producing an ENA. This is done using the direct simulation Monte Carlo (DSMC) method described in the next section.

- Elastic collision with another hydrogen atom, according to the DSMC method described in the next section.

All rates above are from Hodges (1994) for Earth, and average solar conditions, scaled by $(1/0.045)^2$ to account for the larger photon fluxes at the orbital distance of HD 209458b.

The stellar wind density and temperature have also been scaled from average solar conditions for our Sun using relations given by Russell et al. (1988). Given the close proximity of HD 209458b to its host star the choice of stellar wind parameters has to be looked at in some detail. At the Sun we distinguish between slow and fast solar wind, with the former being below about 400 km/s and the latter larger than 400 km/s, often even up to 800 km/s. Although there is temporal fluctuation on all time scales (Wurz 2005), it is for the purpose of this study sufficient to consider average values. Using a proton density of 7 cm^{-3} at Earth orbit translates to about 3500 cm^{-3} at the orbit of HD 209458b using a quadratic scaling. With the radius of HD 209458 being 1.46 times the solar radius, the location of the planet is at $6.6R_{st}$, with R_{st} being the stellar radius. At the Sun, this distance is close to the acceleration region of the solar wind. For the Sun, several measurements show that the acceleration of the solar wind occurs close to the Sun. For the fast solar wind Grall et al. (1996) showed that it is fully developed within $10R_{st}$. These and other measurements have been summarised and compared to theoretical models by Esser et al. (1998). Based on this work we would expect a stellar wind speed at HD 209458b of about 800 km/s. For the slow solar wind there are also measurements of its acceleration. Kohl et al. (1998) show that protons have already 300 km/s at $4R_{st}$, and Sheeley et al. (1997) found similar results with little acceleration beyond $7R_{st}$. Assuming HD 209458b is in the slow solar wind regime the stellar wind velocity would be 300 km/s. Since we do not know what stellar wind regime HD 209458b is actually experiencing, a stellar wind speed of 450 km/s is chosen. Note that for our Sun, the slow solar wind regime is more likely to occur in the ecliptic plane. We can also scale the magnetic field to regions close to the star, which gives a stellar wind magnetic field of $3.5 \mu\text{T}$ using a solar wind magnetic field of 10 nT at 1 AU. That magnetic field, together with the proton density give an Alfvén speed $v_A = 1540 \text{ km/s}$, which suggests that the stellar wind at HD 209458b is sub-alfvénic and a bow shock will not develop (Erkaev et al. 2005).

The photon-hydrogen collision rate, τ_{γ} as shown in Table 1, is chosen lower than a scaled value of $0.6 - 1.6 \text{ s}^{-1}$ averaged over a solar cycle. This was done to approximate the actual velocity-dependent radiation pressure which decreases with velocity for the hydrogen atoms as they move out of the central Lyman- α peak in the velocity spectrum. For the radiation pressure and photoionization event rates, τ , after each time step, for each meta-particle, we draw a random time from an exponential distribution with mean τ , and the event occur if this time is smaller than the time step. Note that we only consider ENAs produced outside the obstacle, so the fluxes presented here are a lower bound. Additional ENAs are produced inside, but including those would require a complete ion flow model.

The forces acting on a hydrogen atom are the gravity of the planet \mathbf{G}_{pl} and of the star \mathbf{G}_{st} .

Because of the rotation, at an angular rate of ω , the fictitious Coriolis, \mathbf{F}_{cor} , and centrifugal, \mathbf{F}_{cent} , forces also affect the hydrogen atoms. The total force, \mathbf{F}_{tot} , on a hydrogen atom is thus

$$\mathbf{F}_{\text{tot}} = \mathbf{G}_{\text{pl}} + \mathbf{G}_{\text{st}} + \mathbf{F}_{\text{cor}} + \mathbf{F}_{\text{cent}}. \quad (1)$$

2.1. Collisions

The collisions between hydrogen atoms are modeled using the direct simulation Monte Carlo (DSMC) method (Bird 1976), where we divide the computational domain into cells. Then after each time step the particles that are in the same cells are considered for hard sphere collisions. From Equation (1.6) in Bird (1976), the frequency of collisions experienced by a single particle is $\nu = n\overline{\sigma v_r}$, where n is the total number density of all species, σ is the total collisional cross-section, and v_r is the relative velocity between the particle and the particles in the surrounding gas. The bar denotes average. From this we get that the total collision frequency in a volume is

$$\frac{1}{2}n\nu = \frac{1}{2}n^2\overline{\sigma v_r} \quad (2)$$

For each pair of particles, their collision probability is proportional to σv_r . For a cell, we estimate n by $N_c N_m / V_c$ where N_c is the number of particles in the cell, N_m is the number of particles per meta-particle, and V_c is the cell volume. If N_m is different for different particles, we must sum all N_m instead of using $N_c N_m$.

To avoid an operation count proportional to N_c^2 , following Garcia (2000, p. 359), we do not directly compute the averages. Instead we estimate a maximum value of σv_r , $(\sigma v_r)_{\text{max}}$, and use that in Equation (2) to compute the number of trials. For each trial we then draw a random pair, and a random number R on $[0, (\sigma v_r)_{\text{max}}]$. If $\sigma v_r > R$ for the chosen pair, the collision is accepted.

The random pair above is uniformly distributed if N_m is the same for all particles, as is the case for these simulations.

2.2. Time Integration

To avoid energy dissipation, the time advance of the particles from time t to time $t + \Delta t$, is done using the symplectic integrators derived by Candy & Rozmus (1991),

$$\mathbf{x} \leftarrow \mathbf{x} + \sum_k c_k \Delta t \mathbf{v}, \quad (3)$$

$$\mathbf{a} \leftarrow \mathbf{a}(\mathbf{x}, t), \quad (4)$$

$$\mathbf{v} \leftarrow \mathbf{v} + \sum_k d_k \Delta t \mathbf{a}, \quad (5)$$

$$t \leftarrow t + \sum_k c_k \Delta t, \quad (6)$$

for $k = 1, \dots, n$. Here \mathbf{x} are the particle positions, \mathbf{v} the velocities, and $\mathbf{a}(\mathbf{x}, t)$ the accelerations. The coefficients c_k and d_k can be found in Candy & Rozmus (1991). The global order of accuracy is n , and $n = 2$ corresponds to the Leapfrog method. In this work we have used $n = 4$.

2.3. Software

We use an existing software, FLASH, developed at the University of Chicago (Fryxell et al. 2000), that provides adaptive grids and is fully parallelized, and that we have extended to do DSMC modeling of planetary exospheres (Holmström 2006). FLASH is a general parallel solver for compressible flow problems. It is written in Fortran 90, well structured into modules, and open source. The parallelization is to a large extent handled by the PARAMESH (MacNeice et al. 2000) library that implements a block-structured adaptive Cartesian grid with the Message-Passing Interface (MPI) library as the underlying communication layer.

2.4. Lyman- α Attenuation

Given the positions of all the hydrogen meta particles at a certain time, we now proceed to compute how they attenuate the stellar Lyman-alpha radiation. We discretize the yz -plane using a grid. For each cell in the grid we compute the velocity spectrum of all hydrogen atoms in the column along the x -axis corresponding to the cell. We then subtract 13 km/s from the x -axis velocity of all atoms to account for the velocity of the star toward the Sun. This velocity spectrum can be converted into a frequency spectrum using the relation $f = f_0 + v/\lambda_0$, where v is the velocity, $\lambda_0 = 1215.67 \cdot 10^{-8}$ cm, and $f_0 = c/\lambda_0$. This spectrum, $h(f)$, is normalized to have unit integral. Assuming only single scattering, the attenuation factor $A(f)$ at each frequency is then given as

$$A(f) = 1 - e^{-ngfah(f)}, \quad (7)$$

where n is the column density, the weighted oscillator strength $gf = 2 \times 0.4162$, and $a = \pi e^2 / (m_e c) = 0.026$ Hz cm². This attenuation factor is then averaged over all columns in the yz -grid, except for those whose center falls outside the projected limb of the star, or inside the planet disc. The projected limb of the star is shifted downward (smaller z) by $4.58 \cdot 10^8$ m to account for the planet orbit's inclination. This attenuation is then applied to the observed spectrum. At each velocity we simply multiply the observed spectrum by the attenuation factor.

3. MODEL RESULTS

We here describe the obtained plasma flow and how well the obtained ENA production fit the HST observations. Using a higher stellar wind velocity than in H08 we get a obstacle shape pointing more radially towards the star. The hydrogen cloud is still cometary shaped but with a

smaller bend compared to results in H08. A slice of the simulations is shown in Figure 2, displaying stellar wind protons and the hydrogen atoms. Visibly we can see that the hydrogen cloud reaches (with significant density) outside the obstacle boundary and can produce ENAs by charge exchange with stellar wind protons. In Figure 3 we also show vectors for the proton flow to illustrate how they are now deflected around the obstacle.

The computed attenuation at mid-transit is shown in Figure 4, where we see that the separation between ENAs and exospheric hydrogen that was visible in the velocity spectrum is also apparent in the attenuation spectrum.

The ENA production is high enough to explain the observed Lyman- α attenuation. Figure 5 shows the resulting attenuation spectra from our model with the default parameter settings along with observational data as reported by Vidal-Madjar et al. (2003). The analysis is focused on the wavelength intervals for which atomic hydrogen absorption has been observed, and where there is no geocoronal observations (Vidal-Madjar et al. 2003). The errors compared to observational data are displayed under these (unshaded) intervals in all attenuation plots that follows. We find that the fit to observations is as good as in H08.

Introducing star gravity and centrifugal force makes particles at smaller radial distances from the star more affected by the gravity of the star than the centrifugal force. The result is that the exosphere between the star and the planet is shifted towards the star, thus increasing the number of exospheric particles outside the obstacle boundary. This increases the number of produced ENAs, shown in Figure 6, but the number of ENAs in the velocity region -130 to 100 km/s is virtually unchanged.

We can also investigate the time dependence of the attenuation. The attenuation as a function of orbital phase is shown in Figure 7. We see that the comet-like hydrogen cloud gives rise to an asymmetry in attenuation over time, making attenuation post-transit higher than pre-transit for an equal time shift. The curve of attenuation over time is in agreement with the observations by Vidal-Madjar et al. (2003), and is also similar to their modeled attenuation curve.

We find it difficult to reproduce the observations without ENA production. If we turn off all ENA production, then we have to increase radiation pressure to get hydrogen with high enough velocity. The resulting attenuation spectrum, shown in Figure 8, significantly differs from the observed one. We can see that the exospheric hydrogen now is accelerated up to velocities of -130 km/s. However, the attenuation is too large, with a sharp drop off around -130 km/s.

3.1. Sensitivity to Exospheric parameters

Since the density and temperature profiles of the exosphere are uncertain we explore a range of values for both these parameters. At our inner boundary the temperature, based on the model by Penz et al. (2008), is approximately half of the temperature estimated by for example Yelle (2004).

For the exospheric density our number is approximately 10 times less than the number estimated by García Muñoz (2007). To study the ENA production as a function of various exospheric conditions we chose 9 different scenarios by testing with higher and lower values for both density and temperature. Exospheric density was varied up and down by a factor of 10 at the inner boundary, where the original density is denoted ρ_0 , giving $\rho_- = \rho_0/10$ and $\rho_+ = 10\rho_0$. Exospheric temperature was varied up and down by a factor of 2 at the inner boundary, and analogously denoted T_0 , $T_- = T_0/2$ and $T_+ = 2T_0$. For each exospheric scenario the only remaining free parameter is the obstacle standoff distance.

Since we here only include ENAs produced outside of the obstacle boundary, exospheric temperature – determining the rate of decrease in density from the exobase, is apparently a more important factor for the ENA production than the exospheric density. Our model is less sensitive to the exospheric density parameter since this parameter can be said to determine only the peak density (at the exobase). The higher sensitivity to exospheric temperature than density can be seen by comparing the attenuation spectra in Figures 9-12. An increase in exospheric density does not effect the attenuation much, even though a decrease in density will reduce the attenuation significantly. In the velocity spectrum a probable cause for this asymmetry: a decreased exospheric density has reduced the number of hydrogen in the studied velocity intervals relatively more than other hydrogen. Using an exospheric temperature with twice the default value we obtain an unreasonably high attenuation, while a decrease in temperature reduces the attenuation considerably.

4. OBSTACLE STANDOFF DISTANCE

Since ENA production depends on the planetary obstacle to the stellar wind, ENA observations can yield information on the obstacle. The size of the magnetosphere of an extrasolar planet cannot be measured directly, but it has implications on many processes. It determines the intensity of planetary radio emission (Desch & Kaiser 1984; Zarka et al. 1997; Farrell et al. 1999; Grießmeier et al. 2007), the protection of the planetary atmosphere against atmospheric loss by the solar wind and by CMEs (Grießmeier et al. 2004; Khodachenko et al. 2007b,a; Lammer et al. 2007), and the protection of a planet against cosmic rays (Grießmeier et al. 2005b, 2008) which in turn can affect biomarker concentrations in the planetary atmosphere (Grenfell et al. 2007, 2008). To improve our understanding of these processes, good estimations for a magnetospheric obstacle would be very helpful. Although model values exist for the size of exomagnetospheres, these models rely on the assumption that the planetary magnetic moment can be modelled in a simple way, which is sometimes disputed. In principle, ENA observations has the potential to discriminate between plausible and less plausible models. To demonstrate this, we here try to derive an approximate size of the magnetosphere and compare the results with those found by magnetospheric modeling.

4.1. Upper Limit on Obstacle Standoff Distance

By using the different exospheric parameters, described in Section 3.1, it is possible to determine an upper limit of the obstacle standoff distance for each set of parameters. We do this by increasing the obstacle standoff distance until it is impossible to get any attenuation with a reasonable stellar wind density. We chose 10000 cm^{-3} as a maximum reasonable stellar wind density and study the attenuation as we increase the obstacle standoff distance by steps of $2 \cdot 10^8$ meters. The obtained upper limits as a function of exospheric parameters are shown in Table 3.

4.2. Estimated Obstacle Standoff Distance

By varying the obstacle standoff distance we should be able to find a best fit for each exospheric scenario. We find that for most scenarios the errors compared to observations are still decreasing when we decrease obstacle distance down to $3 \cdot 10^8$ m. Due to computational limitations it is beyond the scope of this work to do simulations with an inner boundary below $2.7 \cdot 10^8$ m. We can therefore not find the value with best fit for most scenarios but can state that the value is $\leq 3 \cdot 10^8$ m. The best fit to observations for each exospheric scenario is shown in Table 4.

4.3. Comparison of Obstacle Distances to Magnetospheric Modeling

The magnetosphere is shaped by the interplay between the stellar wind flow and the planetary magnetic field. The size of the magnetosphere depends on the magnetic pressure (planetary magnetic field plus the field generated by the magnetopause currents) inside the magnetosphere and the stellar wind ram pressure outside the magnetosphere (Voigt (1995); Grießmeier et al. (2007)). The contribution of other factors in the pressure balance (e.g. the thermal pressure) is negligible in the present case. In term of units normalized to Jupiter’s units, the magnetospheric standoff distance $R_{\mathcal{M}}$ can then be written as:

$$R_{\mathcal{M}} \approx 40R_{Jup} \left[\frac{\widetilde{\mathcal{M}}^2}{\widetilde{n}\widetilde{v_{rel}}^2} \right]^{1/6}. \quad (8)$$

Here, $\widetilde{\mathcal{M}}$ is the planetary magnetic dipole moment in units Jupiter’s magnetic moment (which is taken as $\mathcal{M}_{Jup} = 1.56 \cdot 10^{27} \text{ Am}^2$ (Cain et al. 1995)). Similarly, the stellar wind velocity and density are taken relative to the values encountered at Jupiter’s orbit: $\widetilde{n} = n/n_{Jup}$ and $\widetilde{v_{rel}} = v_{rel}/v_{rel,Jup}$, with $n_{Jup} = 2.0 \cdot 10^5 \text{ m}^{-3}$, and $v_{rel,Jup} = 520 \text{ km/s}$. The index ”rel” for the stellar wind velocity is a reminder that we use the relative stellar wind velocity as seen from the planet (i.e. including the aberration effect by the planetary orbital velocity, cf. Section 2).

Taking the stellar wind parameters from Table 1, the magnetic moment is the only remaining

free parameter required to obtain $R_{\mathcal{M}}$. Conversely, the values obtained for $R_{\mathcal{M}}$ in the previous section (Tables 3 and 4) allow us to test and constrain existing models on planetary magnetic moments. This is especially important as two different ideas exist: According to the first, the strength of the planetary magnetic dipole moment can be estimated from the planetary characteristics using simple scaling relations. This approach was taken e.g. Farrell et al. (1999); Lazio et al. (2004); Grießmeier et al. (2004, 2005a, 2007); Stevens (2005). The second approach relies on numerical simulations of magnetic dynamos. Such numerical experiments indicate that the magnetic moment may be independent on the angular frequency (Christensen & Aubert 2006; Olson & Christensen 2006). See also Cain et al. (1995) for a critical analysis of magnetic moment scaling laws.

Table 5 shows the size of the magnetospheric obstacle for various values of the planetary magnetic moment. We choose labels S1–S3 for values of the planetary magnetic moment that are obtained by the assumption that the planetary rotation has a strong influence on the planetary magnetic moment. Labels N1–N3 are used for cases which assume that HD 209458b is rapidly rotating. As the magnetic moment scaling laws are based on Jupiter, this is equivalent to saying that rotation rate has no influence on the magnetic dipole moment. Finally we have, to enable a comparison, calculated which magnetic moment the values in Tables 3 and 4 would correspond to. These values are labeled C1–C3. It is worth mentioning that, according to Equation (8), the stellar wind parameters influence $R_{\mathcal{M}}$ only with a low exponent, and the result is thus not very sensitive to the choice of stellar wind parameters. For example, taking the stellar wind parameters of Grießmeier et al. (2007) rather than those of Table 1 modifies the numerical values in Table 5 by less than 10%.

The values of Table 5 can now be compared to those of Tables 3 and 4. The comparison with Table 3 gives us that the magnetic moment of HD 209458b can be constrained to $5\mathcal{M}_{Jup}$ regardless of exospheric scenarios. And we also see that most scenarios would establish the magnetic moment of HD 209458b as smaller than \mathcal{M}_{Jup} . The comparison with Table 4 shows that, with the current uncertainties on exospheric conditions, none of the cases S1–S3 and N1–N3 can currently be ruled out. However, if the exospheric conditions were certain a comparison would indicate which cases of planetary magnetic moments, S1–S3 or N1–N3 in Table 5, are more likely. If for example our default exospheric parameters are approximately correct we would have an estimation of the magnetic moment of HD 209458b as $\approx 0.4\mathcal{M}_{Jup}$. Within error margins, this value is compatible with the following interpretations: (a) planetary rotation is important for magnetic moment generation, but the true magnetic moment is close to the maximum value of the range predicted by the different scaling laws (case S3 in Table 5), or (b) planetary rotation is not as important as previously thought (cases N1–N3).

5. CONCLUSIONS

Holmström et al. (2008) showed that the production of energetic neutral atoms (ENAs) around HD 209458b can explain the observations reported by Vidal-Madjar et al. (2003). This work does

a more detailed study of the ENA production around HD 209458b. Using an improved plasma flow model we model the ENA production from charge-exchange between stellar wind protons and exospheric hydrogen outside the obstacle boundary under stellar wind conditions similar to those at our Sun. Given uncertainties of the exospheric parameters we investigate their relative influence on the ENA production and determine an upper bound on the obstacle standoff distance for different values of exospheric density and temperature.

We find that the improved and more accurate flow model presented here further supports ENAs as the explanation for the observed atomic hydrogen around HD 209458b. Using the expected stellar wind parameters we are able to reproduce the comet-like hydrogen cloud and the observed attenuation spectra during transit. The absorption of atomic hydrogen as reported in Vidal-Madjar et al. (2003) can thus be explained by theory and conditions derived from our solar system. What is different from our solar system is however a close-in Jupiter type planet, and from the ENA observations we try to extract information about the planet. The exospheric conditions and magnetic moment of HD 209458b are uncertain, and we study the ENA production for different exospheric conditions. We find that exospheric temperature is a more critical factor for the ENA production than exospheric density. If exospheric conditions were determined, the only remaining free parameter would be the obstacle standoff distance. For our assumed default exosphere we find that an obstacle standoff distance of $4 \cdot 10^8$ m gives a good fit to observations. Depending on exospheric parameters an upper bound of the obstacle standoff distance is found at $(4-10) \cdot 10^8$ m. Comparing the obtained obstacle standoff distances for the respective exospheric scenarios we see that the ENA observations could also provide information for exomagnetospheric modeling. Our simulations also show that the majority of tested exospheric scenarios would, with the available ENA observations, determine the magnetic moment of HD 209458b to smaller than that of Jupiter. With our default parameters we estimate the magnetic moment of HD 209458b to be approximately 40 per cent of Jupiter’s magnetic moment. The currently available data are not yet sufficient to put good limits on planetary magnetic moments. However, it seems possible that a more detailed modeling of exospheric conditions, together with improved ENA observations, could help to clarify the role of planetary rotation in the generation of planetary magnetic fields in the future.

The software used in this work was in part developed by the DOE-supported ASC /Alliance Center for Astrophysical Thermonuclear Flashes at the University of Chicago, USA. This research was conducted using the resources of LUNARC, Lund University, Sweden and HPC2N, Umeå University, Sweden.

This study was carried out within the framework of the International Space Science Institute team Evolution of Exoplanet Atmospheres and their Characterization. The authors also thank various experts within the Europlanet N2 discipline working groups DWG1 and DWG7 for stimulating discussions on the studied topic. T.P. is supported by the Marie Curie Fellowship project ISHERPA and the host institution INAF Osservatorio Astronomico di Palermo.

REFERENCES

- Bird, G. A. 1976, *Molecular gas dynamics* (Oxford, UK: Clarendon Press)
- Cain, J. C., Beaumont, P., Holter, W., Wang, Z., & Nevanlinna, H. 1995, *J. Geophys. Res.*, 100, 9439
- Candy, J., & Rozmus, W. 1991, *J. of Comput. Phys.*, 92, 230
- Charbonneau, D., Brown, T. M., Latham, D. W., & Mayor, M. 2000, *ApJ*, 529, L45
- Christensen, U. R., & Aubert, J. 2006, *Geophysical J. Int.*, 166, 97
- Collier, M., et al. 2001, *J. Geophys. Res.*, 106, 24893
- Desch, M. D., & Kaiser, M. L. 1984, *Nature*, 310, 755
- Erkaev, N. V., Penz, T., Lammer, H., Lichtenegger, H. I. M., Biernat, H. K., Wurz, P., Grießmeier, J.-M., Weiss, W. W. 2005, *ApJS*, 157, 396
- Esser, R., Edgar, R. J., & Brickhouse, N. S. 1998, *ApJ*, 498, 448
- Farrell, W. M., Desch, M. D., & Zarka, P. 1999, *J. Geophys. Res.*, 104, 14025
- Fryxell, B., et al. 2000, *ApJS*, 131, 273
- Futaana, Y., et al. 2006, *Icarus*, 182, 413
- Galli, A., et al. 2008, *Planet. Space Sci.*, 56, 807
- Garcia, A. L. 2000, *Numerical methods for physics* (Upper Saddle River, N.J., USA: Prentice Hall)
- García Muñoz, A. 2007, *Planet. Space Sci.*, 55, 1426
- Grall, R. R., Coles, W. A., KlingleSmith, M. T., Breen, A. R., Williams, P. J. S., Markkanen, J., & Esser, R. 1996, *Nature*, 379, 429
- Grenfell, J. L., et al. 2007, *Astrobiology*, 7, 208
- Grenfell, J. L., Grießmeier, J.-M., Patzer, B., Rauer, H., Stracke, B., & von Paris, P. 2008, *Astrobiology*, Submitted
- Grießmeier, J.-M., Motschmann, U., Mann, G., & Rucker, H. O. 2005a, *A&A*, 437, 717
- Grießmeier, J.-M., Stadelmann, A., Grenfell, J. L., Lammer, H., & Motschmann, U. 2008, *Icarus*, Submitted
- Grießmeier, J.-M., Stadelmann, A., Motschmann, U., Belisheva, N. K., Lammer, H., & Biernat, H. K. 2005b, *Astrobiology*, 5, 587

- Griebmeier, J.-M., et al. 2004, *A&A*, 425, 753
- Griebmeier, J.-M., Zarka, P., & Spreeuw, H. 2007, *A&A*, 475, 359
- Henry, G. W., Marcy, G. W., Butler, R. P., & Vogt, S. S. 2000, *ApJ*, 529, L41
- Hodges, R. R. J. 1994, *J. Geophys. Res.*, 99, 23229
- Holmström, M. 2006, *Space Sci. Rev.*, 126, 435.
- Holmström, M., Ekenbäck, A., Selsis, F., Penz, T., Lammer, H., & Wurz, P. 2008, *Nature*, 451, 970
- Khodachenko, M. L., et al. 2007a, *Planet. Space Sci.*, 55, 631
- Khodachenko, M. L., et al., *Astrobiology*, 7, 167
- Kohl, J. L., et al. 1998, *ApJ*, 501, 127
- Lammer, H., et al. 2007, *Astrobiology*, 7, 185
- Lazio, T. J. W., Farrell, W. M., Dietrick, J., Greenless, E., Hogan, E., Jones, C., & Hennig, L. A. 2004, *ApJ*, 612, 511
- Lindsay, B. G., & Stebbings, R. F. 2005, *J. Geophys. Res.*, 110, A12213
- MacNeice, P., Olson, K., Mobarry, C., deFainchtein, R., & Packer, C. 2000, *Comput. Phys. Communications*, 126, 330
- Olson, P., & Christensen, U. R. 2006, *Earth and Planet. Sci. Lett.*, 250, 561
- Penz, T., et al. 2008, *Planet. Space Sci.*, 56, 1260
- Russell, C. T., Baker, D. N., & Slavin, J. A. 1988, *The magnetosphere of Mercury (Mercury, University of Arizona Press)*, 514
- Sheeley, N. R., Jr., et al. 1997, *ApJ*, 484, 472
- Stevens, I. R. 2005, *MNRAS*, 356, 1053
- Vidal-Madjar, A., des Etangs, A. L., Désert, J.-M., Ballester, G. E., Ferlet, R., Hébrard, G., & Mayor, M. 2003, *Nature*, 422, 143
- Vidal-Madjar, A., et al. 2004, *ApJ*, 604, L69.
- Voigt, G-H. 1995 in *Handb. of Atmos. Electrodynamics*, ed H. Volland (CRC Press), 333
- Wurz, P. 2005, in *The Dynamic Sun: Challenges for Theory and Observations*, (ESA), vol. ESA SP-600, chap. 5.2
- Yelle, R. V. 2004, *Icarus*, 170, 167

Zarka, P., et al. 1997 in *Ground-based High Sensitivity Radio Astron. at Decameter Wavelengths*, ed H.O. Rucker, S.J. Bauer & A. Lecacheux (Austrian Academy of Sciences Press, Vienna), 101

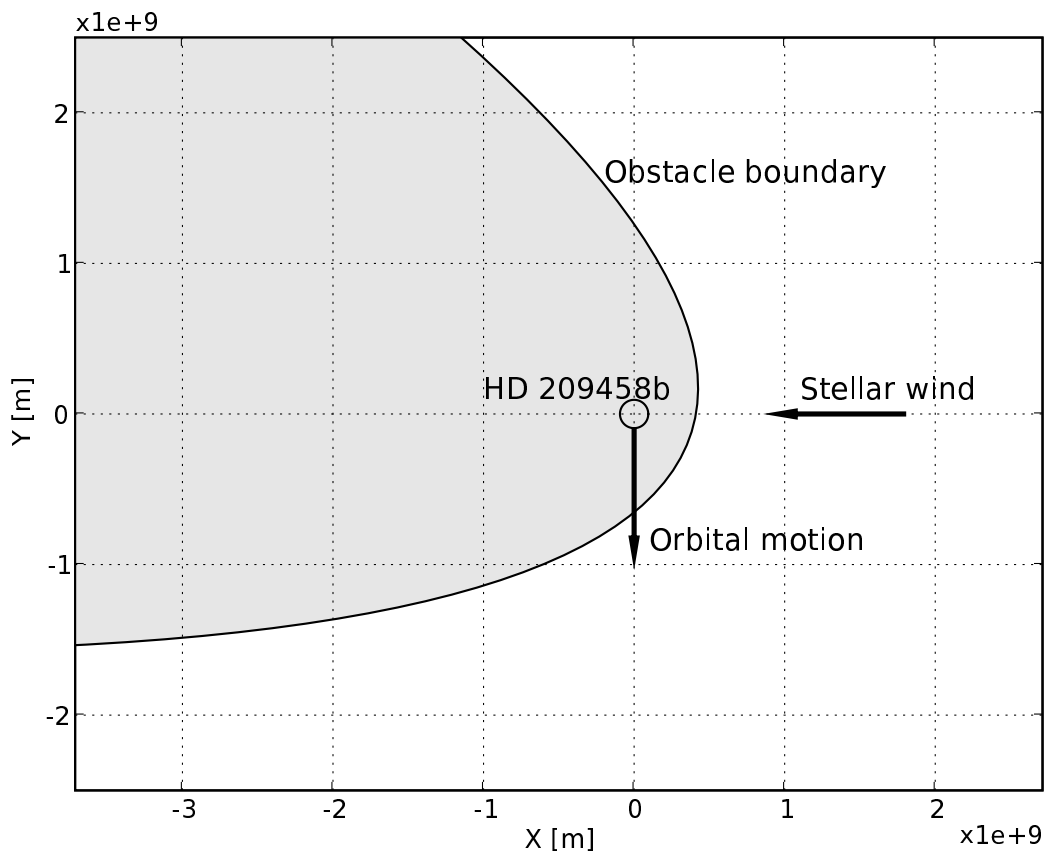


Fig. 1.— Illustration of near-planet geometry and the ENA production region. This work only considers ENAs produced outside of the obstacle boundary – a magnetopause in case HD 209458b has an intrinsic magnetic field or an induced magnetospheric boundary otherwise – which is the unshaded area. The plot shows the shape of the obstacle boundary for the default parameters as in Table 1.

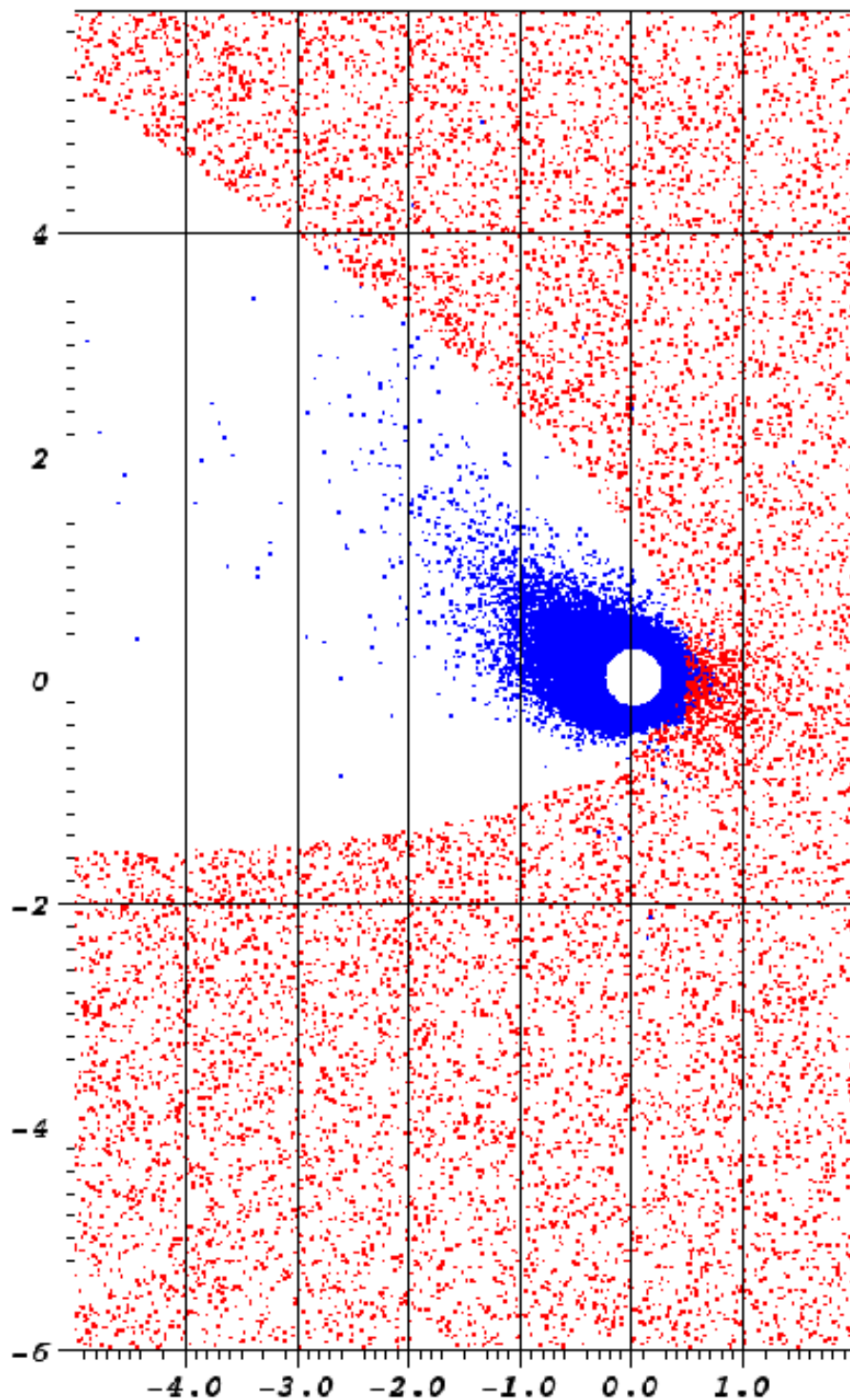


Fig. 2.— The flow of stellar wind protons and the exospheric hydrogen cloud seen from above in the direction of the negative z -axis (perpendicular to the orbital plane). Each point corresponds to a neutral hydrogen (red), or a proton (blue) meta particle in the slice $-10^7 \leq z \leq 10^7$ m. The scale on the axes are 10^9 m. The circle without particles correspond to the inner boundary of the simulation, and the large area without protons corresponds to the assumed obstacle to the stellar wind, on which the protons are reflected.

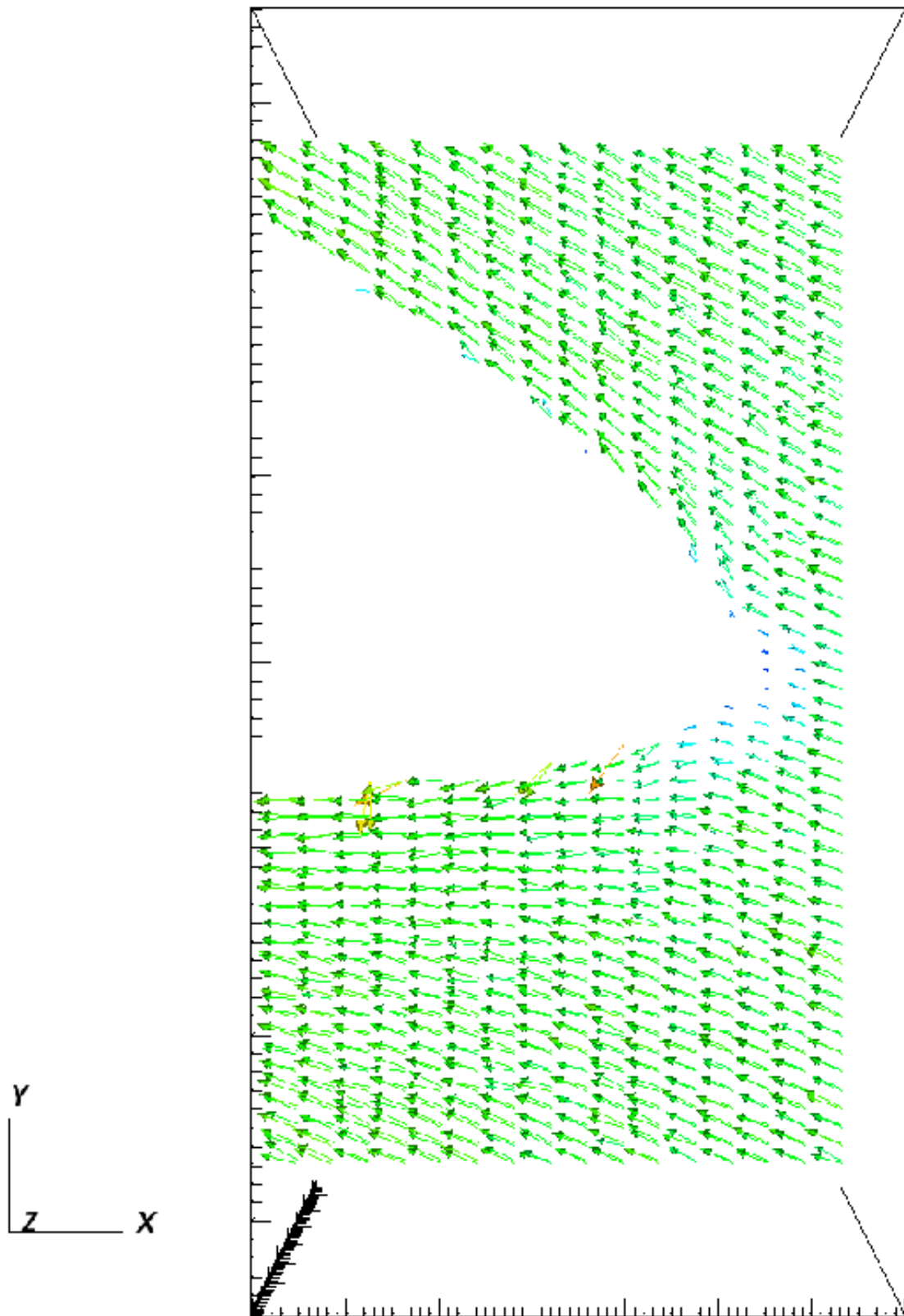


Fig. 3.— Velocity vectors of stellar wind protons in the orbital plane.

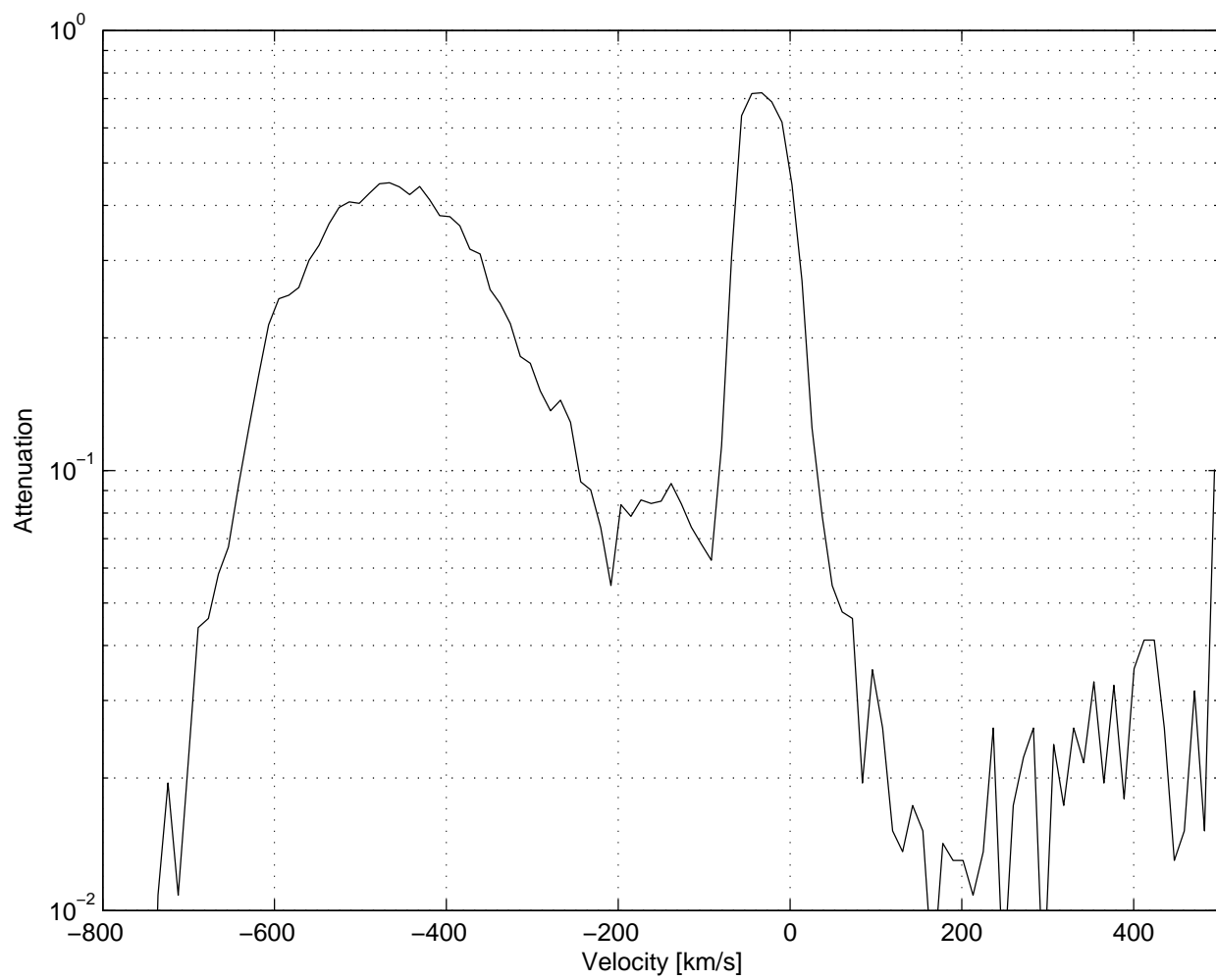


Fig. 4.— The attenuation at mid-transit as a function of hydrogen x -axis velocity, computed with Eq.(7).

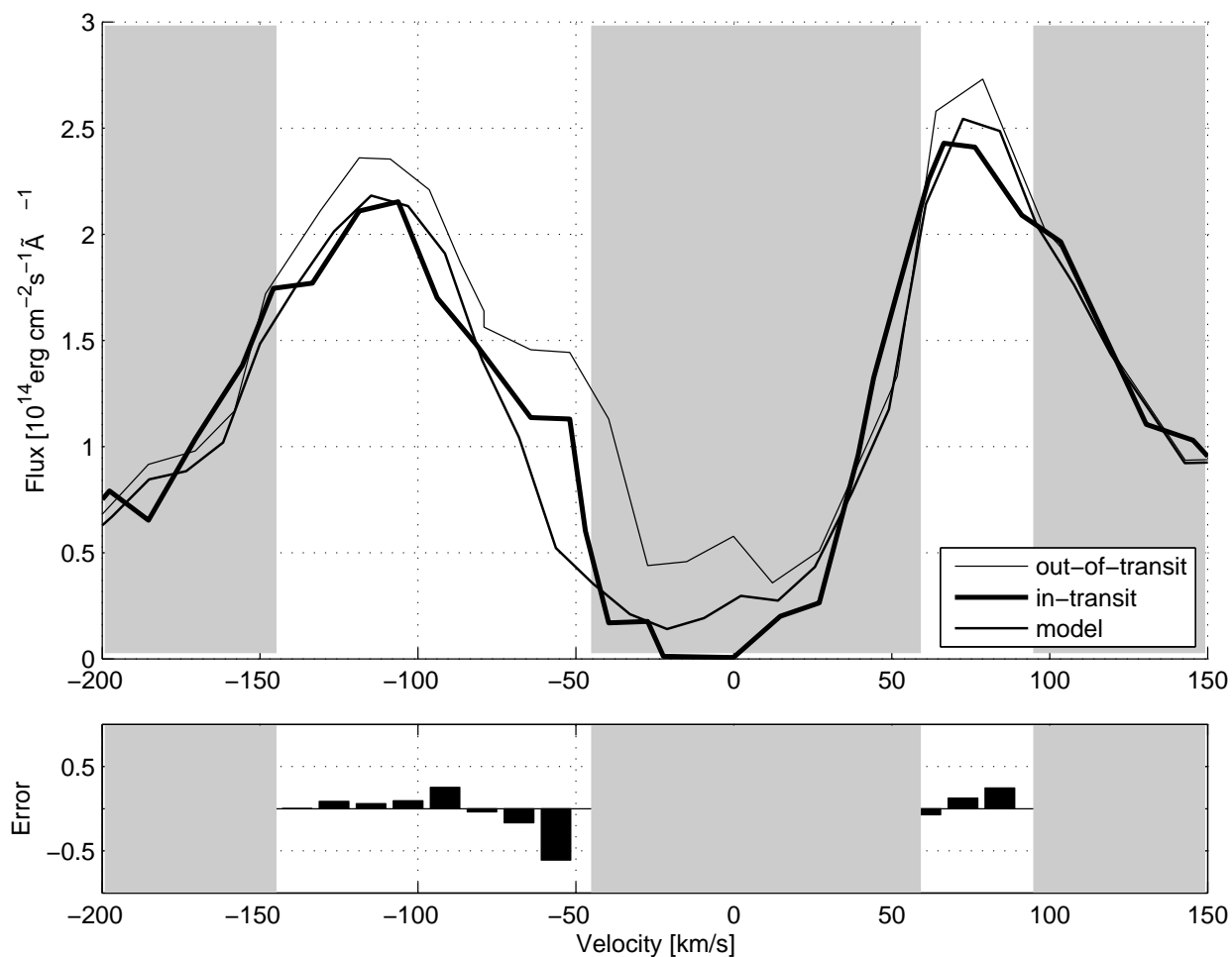


Fig. 5.— The obtained attenuation spectrum and comparison with observations. In light grey is the observed profile before transit. In black is the observed profile during transit. In dark grey is the modeled profile, constructed by applying the attenuations computed from the simulations to the observed profile before transit. The modeled profile is computed at the instant of mid-transit.

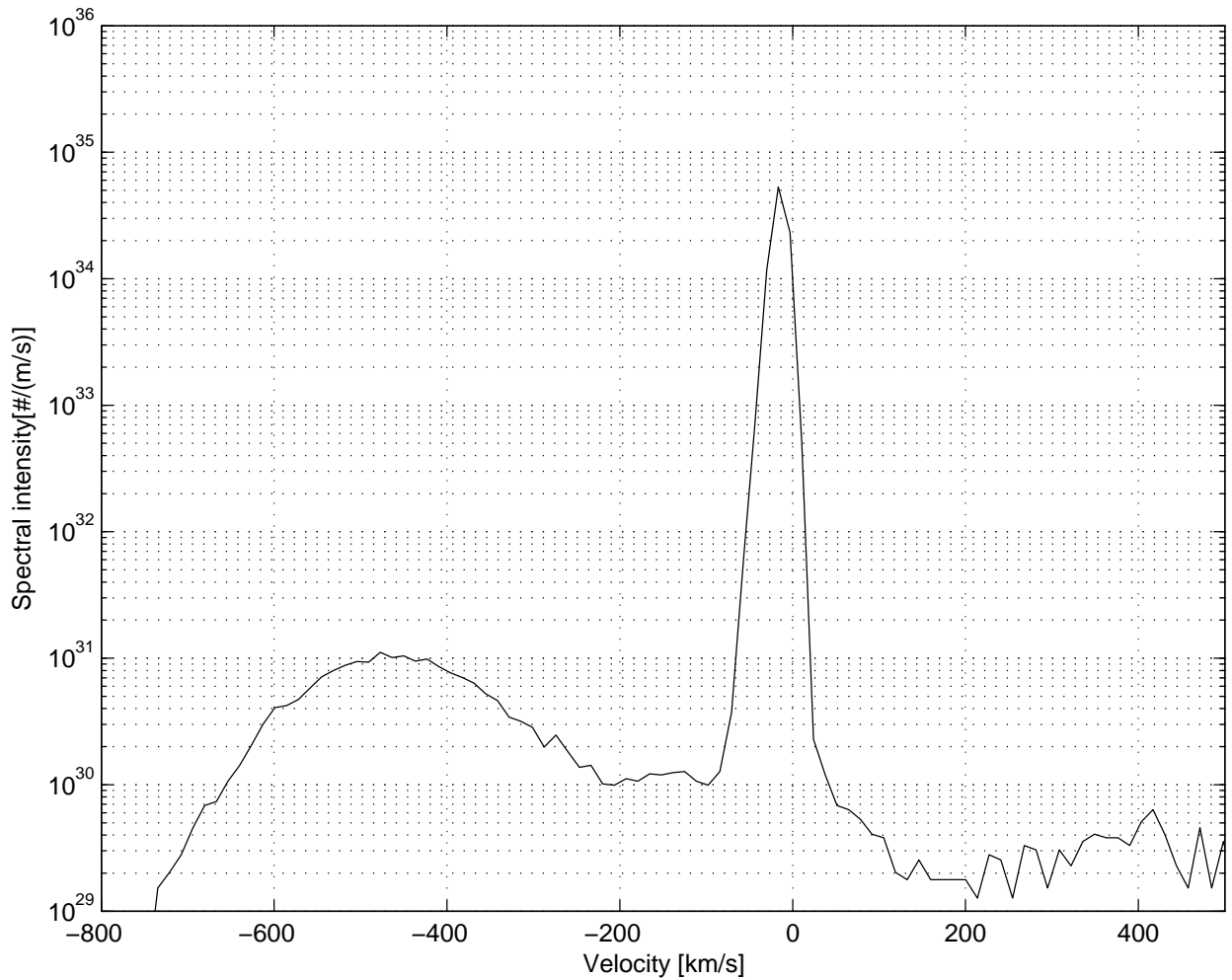


Fig. 6.— Velocities of the hydrogen atoms. The modeled x -axis (planet–star) velocity spectrum of hydrogen atoms in front of the star at the moment of mid transit, not including atoms in front or behind the planet. The low-velocity hydrogen, seen as a peak in the spectrum between -75 to 25 km/s, are purely exospheric but the rest of the spectrum displays large number of ENAs produced by charge-exchange with the stellar wind.

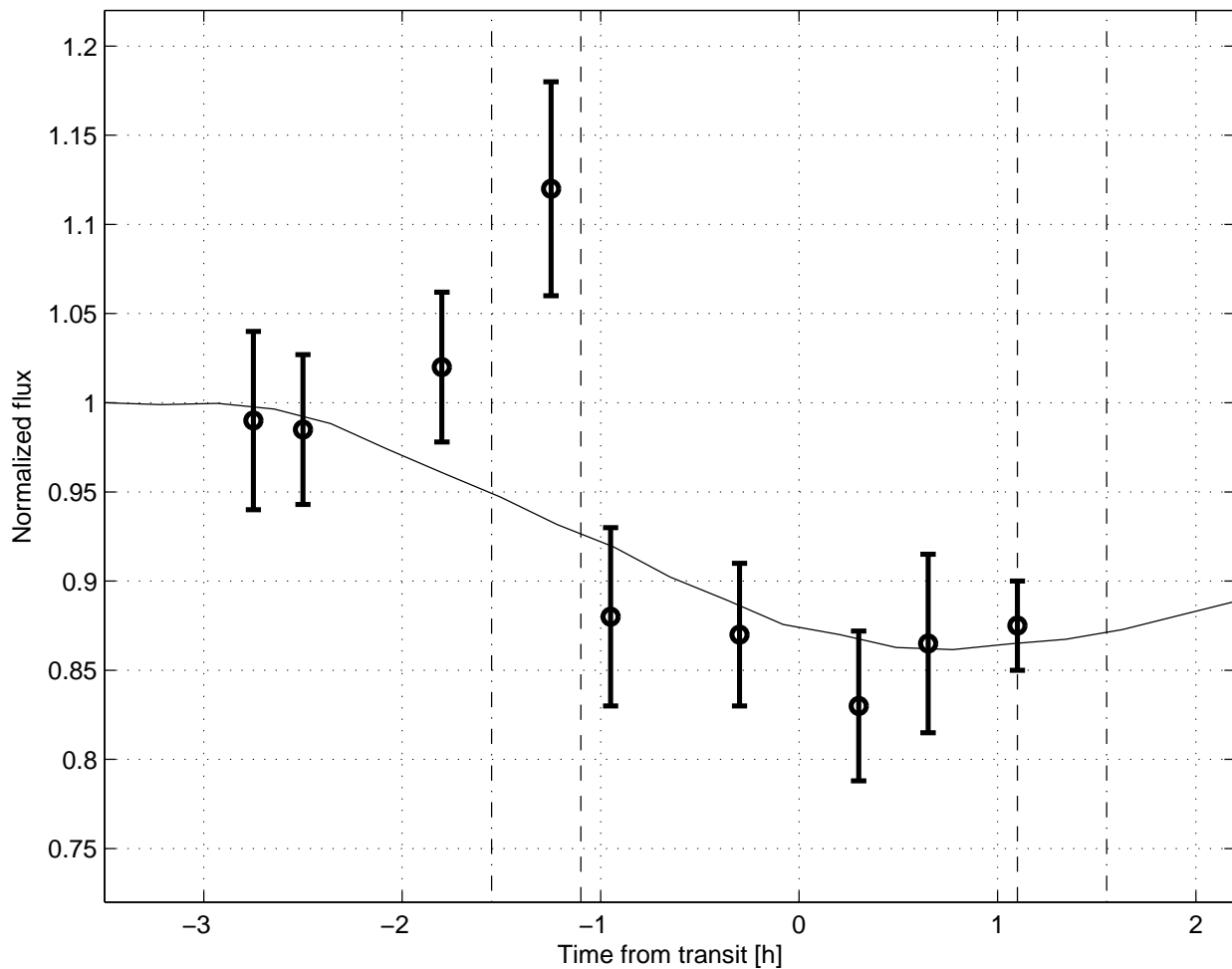


Fig. 7.— Relative flux of Lyman α as a function of HD 209458’s system phase. Time is centered around mid-transit. The curve is the attenuation as obtained by our model, and circles with error bars are observational data as reported by Vidal-Madjar et al. (2003). The dashed lines mark the first and second contact at the beginning and end of the transit.

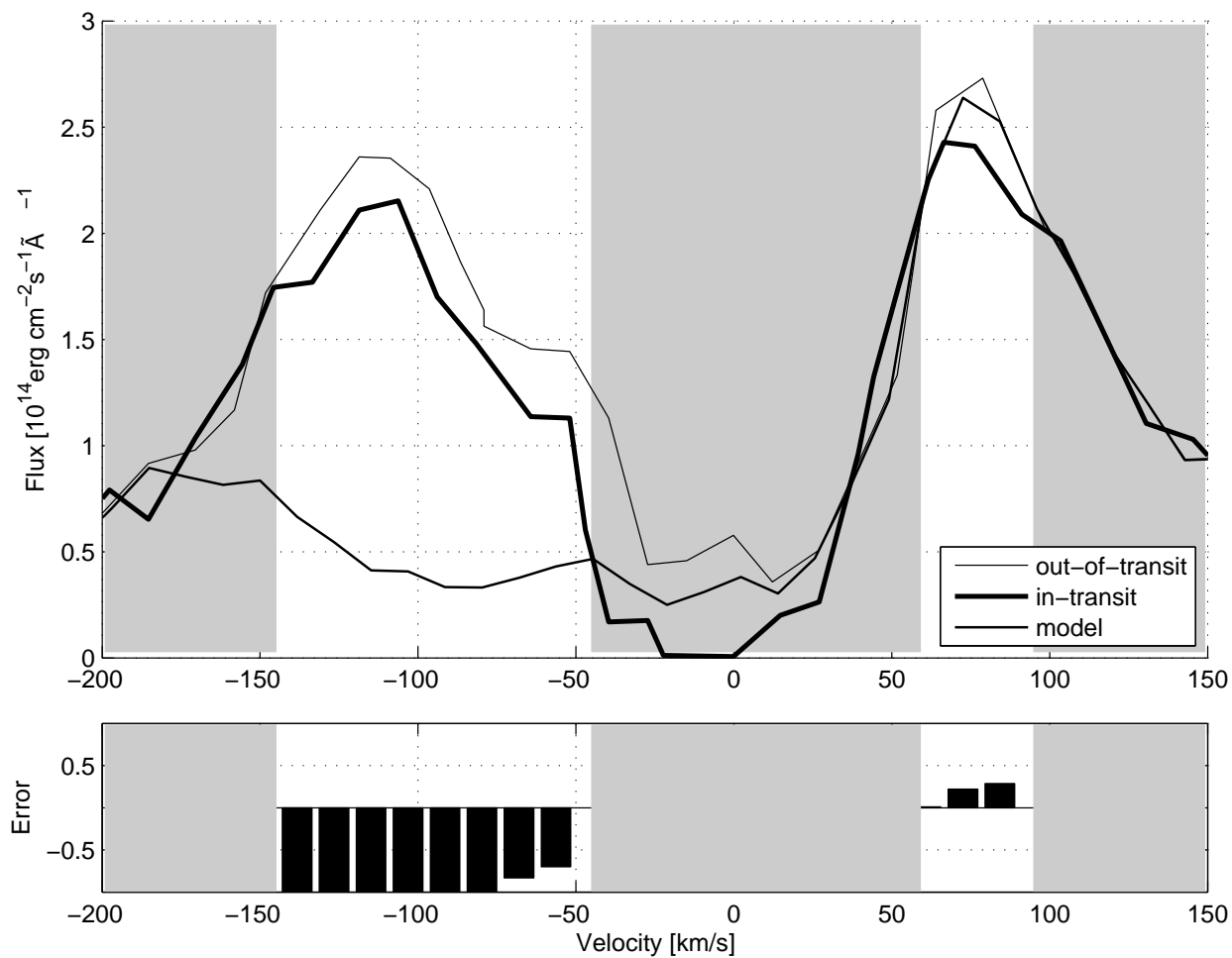


Fig. 8.— The attenuation spectrum with no ENA production and, to accelerate the hydrogen atoms to 130 km/s, a larger radiation pressure corresponding to a photon collision rate of 1.4 s^{-1} .

Table 1. Default values of physical parameters, and values of constants used in the simulations, unless otherwise noted. A star (*) indicates a value different from HO08.

| Name | Symbol | Value | |
|---|----------|---|-----------------|
| Star radius | ... | $7.0 \cdot 10^8$ m | $= R_{Sun}$ |
| Planet radius | R_p | $9.4 \cdot 10^7$ m | $= 1.3 R_{Jup}$ |
| Planet mass | ... | $1.3 \cdot 10^{27}$ kg | $= 0.7 M_{Jup}$ |
| Orbital distance | ... | $6.7 \cdot 10^9$ m | $= 0.045$ AU |
| Orbital velocity | ... | $1.4 \cdot 10^5$ m/s | ... |
| Angular velocity | ω | $2 \cdot 10^{-5}$ rad/s | ... |
| Inner boundary radius* | R_0 | $2.7 \cdot 10^8$ m | $= 2.8 R_p$ |
| Inner boundary temperature* | ... | $0.6 \cdot 10^4$ K | ... |
| Inner boundary density* | n | $4 \cdot 10^{13}$ m ⁻³ | ... |
| H-H cross-section | ... | 10^{-21} m ² | ... |
| H-H ⁺ cross-section ^a | ... | $\approx 2 \cdot 10^{-19}$ m ² | ... |
| UV absorption rate | τ_r | 0.35 s ⁻¹ | ... |
| Photoionization rate | τ_i | $7 \cdot 10^{-5}$ s ⁻¹ | ... |
| Obstacle standoff distance | X_0 | $4 \cdot 10^8$ m | $= 4.3 R_p$ |
| Stellar wind density* | ... | $3.5 \cdot 10^9$ m ⁻³ | ... |
| Stellar wind velocity* | u_{sw} | $4.5 \cdot 10^5$ m/s | ... |
| Stellar wind temperature | T_{sw} | $1 \cdot 10^6$ K | ... |

^aEnergy dependent from Lindsay & Stebbings (2005)

Table 2. Default numerical parameter values used in the simulations. A star (*) indicates a value different from HO08.

| Name | Symbol | Value |
|--|------------|----------------------|
| ... | x_{\min} | $-5.0 \cdot 10^9$ m |
| ... | x_{\max} | $2.0 \cdot 10^9$ m |
| ... | y_{\min} | $-7.0 \cdot 10^9$ m |
| ... | y_{\max} | $7 \cdot 10^9$ m |
| ... | z_{\min} | $-3.5 \cdot 10^9$ m |
| ... | z_{\max} | $3.5 \cdot 10^9$ m |
| Number of particles per meta-particle* | N_m^a | $3.44 \cdot 10^{32}$ |
| Number of cells | ... | $16 \cdot 10^6$ |
| Final time | t_{\max} | 10^5 s |
| Time step | Δt | 25 s |

^aWe tried to keep the total number of meta particles relatively independent of exospheric density. N_m therefore changed with approximately $1/\Delta_\rho$ for the different exospheric scenarios (see Section 3.1), where Δ_ρ is the change in the exospheric density.

Table 3. Obtained upper bounds for obstacle stand-off distance as a function of exosphere density and temperature. The lengths are given in 10^8 m.

| $\rho_- T_-$ | $\rho_- T_0$ | $\rho_- T_+$ | $\rho_0 T_-$ | $\rho_0 T_0$ | $\rho_0 T_+$ | $\rho_+ T_-$ | $\rho_+ T_0$ | $\rho_+ T_+$ |
|--------------|--------------|--------------|--------------|--------------|--------------|--------------|--------------|--------------|
| 4 | 6 | 8 | 6 | 6 | 10 | 6 | 6 | 8 |

Table 4. Estimated obstacle standoff distance for each exospheric scenario. The lengths are given in 10^8 m.

| $\rho_- T_-$ | $\rho_- T_0$ | $\rho_- T_+$ | $\rho_0 T_-$ | $\rho_0 T_0$ | $\rho_0 T_+$ | $\rho_+ T_-$ | $\rho_+ T_0$ | $\rho_+ T_+$ |
|--------------|--------------|--------------|--------------|--------------|--------------|--------------|--------------|--------------|
| $\leq 3^a$ | $\leq 3^a$ | $\leq 3^a$ | $\leq 3^a$ | 4 | 6 | $\leq 3^a$ | 4 | 6 |

^aAn entry of ≤ 3 means that a better fit could probably be found by decreasing the obstacle standoff below $3 \cdot 10^8$ m. Such simulations would not be accurate with the current model since we have used an inner boundary of $2.7 \cdot 10^8$ m.

Table 5. Magnetospheric standoff distance for various values of the planetary magnetic moment (in units of Jupiter’s magnetic moment).

| case | $\widetilde{\mathcal{M}}$ | $R_{\mathcal{M}} [R_p]$ | $R_{\mathcal{M}} [10^8 \text{ m}]$ |
|-----------------|---------------------------|-------------------------|------------------------------------|
| S1 ^a | 0.05 | 2.3 | 2.2 |
| S2 | 0.09 | 2.8 | 2.7 |
| S3 | 0.17 | 3.5 | 3.3 |
| N1 ^b | 0.43 | 4.7 | 4.0 |
| N2 | 0.46 | 4.8 | 4.5 |
| N3 | 0.49 | 5.0 | 4.7 |
| C1 ^c | 1.0 | 6.3 | 5.9 |
| C2 | 2.5 | 8.5 | 8.0 |
| C3 | 4.9 | 11 | 10 |

^aCases S1–S3 are obtained with the formalism described in Grießmeier et al. (2007). They represent the minimum, (geometrical) average and maximum value expected for a tidally locked planet.

^bCases N1–N3 are obtained with the same formalism, but assuming that the planet is rapidly rotating (i.e. with the same angular velocity as Jupiter).

^cThe last cases C1–C3 are probably unrealistically high. They were calculated for comparison with Tables 3 and 4.

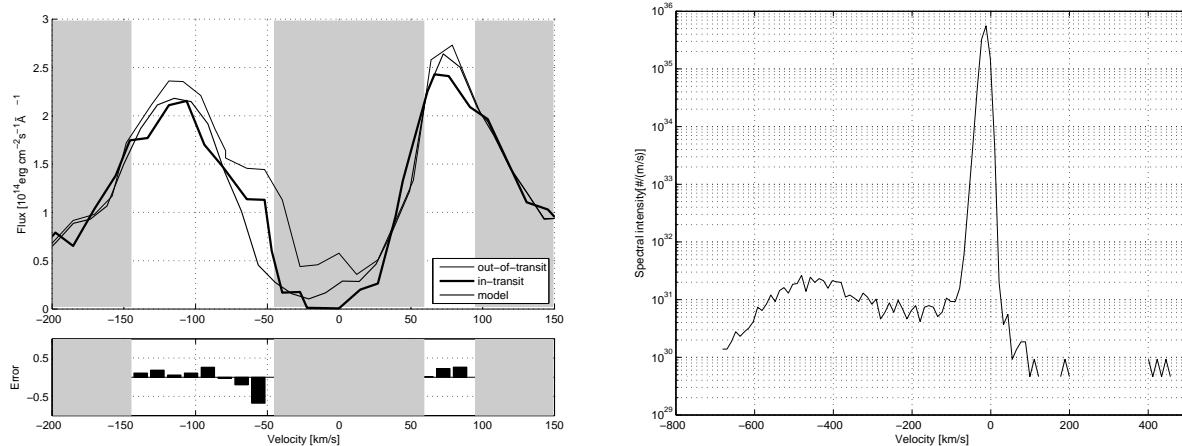


Fig. 9.— The effects to the attenuation and velocity spectra when increasing the exospheric density by a factor 10.

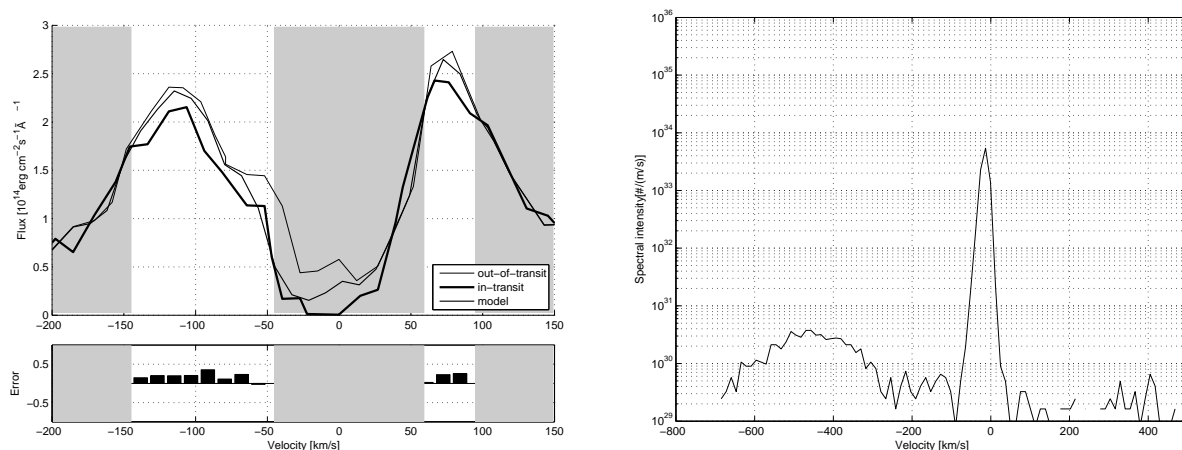


Fig. 10.— The effects to the attenuation and velocity spectra when decreasing the exospheric density by a factor 10.

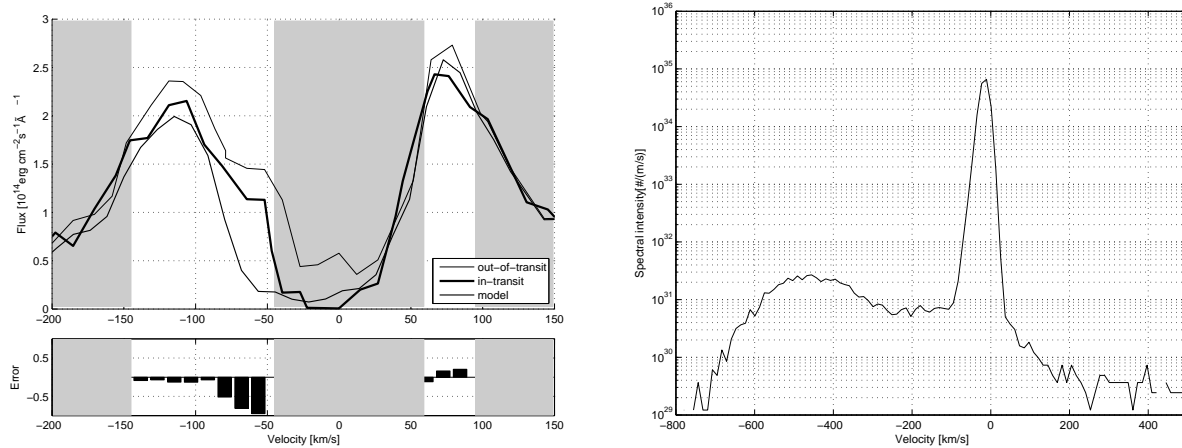


Fig. 11.— The effects to the attenuation and velocity spectra when increasing the exospheric temperature by a factor 2.

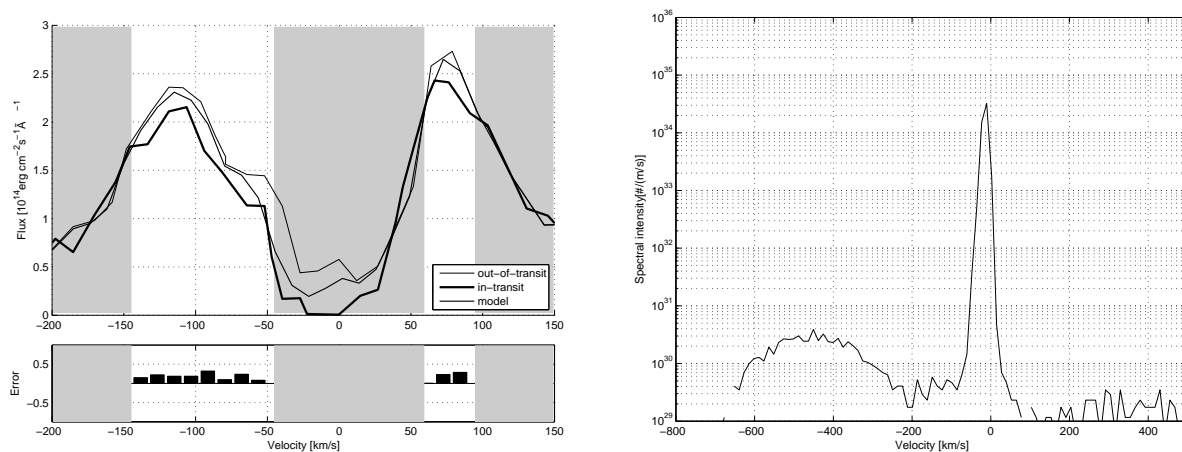


Fig. 12.— The effects to the attenuation and velocity spectra when decreasing the exospheric temperature by a factor 2.